Thermal stability and phase transformation of semi-crystalline mesostructured TiO2 in the presence of heteroelements

Florian Jonas, Bénédicte Lebeau, Laure Michelin, Cédric Carteret, Ludovic Josien, Loïc Vidal, Séverinne Rigolet, Pierrick Gaudin, Jean-Luc Blin

Thermal stability and phase transformation of semi-crystalline mesostructured TiO_2 in the presence of heteroelements

Florian Jonas[1], Bénédicte Lebeau[2,3*], Laure Michelin[2,3], Cédric Carteret[4], Ludovic Josien[2,3], Loïc Vidal[2,3], Séverinne Rigolet[2,3], Pierrick Gaudin[1], Jean-Luc Blin[1*],

[1]: Université de Lorraine, CNRS, L2CM, F-54000 Nancy, France
[2] : Université de Haute Alsace (UHA), CNRS, IS2M UMR 7361, F-68100 Mulhouse, France
[3] : Université de Strasbourg, F-67000 Strasbourg, France
[4] : Université de Lorraine, CNRS, LCPME, F-54000 Nancy, France
[5] : Université de Poitiers, CNRS, IC2MP, UMR 7285, 86073 Poitiers Cedex 9 France.

* Corresponding authors :

Pr. Jean-Luc Blin
Université de Lorraine
L2CM UMR 7053
Faculté des Sciences et Technologies
BP 70239
F-54506 Vandoeuvre-lès-Nancy cedex, France
Tel. +33 3 83 68 43 70
E-mail: Jean-Luc.Blin@univ-lorraine.fr

Dr. Bénédicte Lebeau
Université de Haute Alsace (UHA), CNRS, Axe Matériaux à Porosité Contrôlée (MPC), Institut de Science des Matériaux de Mulhouse (IS2M), UMR 7361, ENSCMu
3bis rue Alfred Werner
F-68093 Mulhouse cedex, France
Tel. +33 3 89 33 68 82
E-mail: Benedicte.Lebeau@uha.fr

Abstract

The effect of the introduction of heteroelement (Si, P, Al, Ge, Ga and Zr) by direct synthesis on the thermal stability of mesostructured titania prepared by the soft templating pathway has been investigated. All materials have been surfactant-extracted with EtOH and calcined at different temperatures up to 900°C. Ti^{4+} can be partially substituted by most of the investigated heteroelements but they mainly form an oxide amorphous phase surrounding the titania anatase particles. Results obtained by SAXS, X-Ray diffraction, Raman spectroscopy and manometry nitrogen adsorption-desorption show that the crystallization of the amorphous titania into nanosized anatase particles and the transition from anatase to rutile occur at higher temperature with the addition of the heteroelement. Even if the lattice distortion introduced by the partial Ti^{4+} substitution can participate to this phenomenon, it is mainly due the «glass» effect induced by the presence of the heteroelement in the TiO_2 amorphous phase, which limits the growth of the nanosized anatase crystallites. However, when the crystallites reach a limit size, the collapse of the mesostructure occurs. With increasing the calcination temperature, the anatase titania particles become bigger and bigger, the transition from anatase to rutile takes place and the heteroelement can crystallize or be integrated in a crystalline phase. Among the considered heteroelements and by comparison with the bare mesostructured TiO_2, the most beneficial effect is obtained in the presence of Si^{4+} and PO_4^{3-} for which the mesostructure collapse at higher temperature by about two hundred Celsius degrees. Al^{3+} and Ge^{4+} enhance the thermal stability by about a hundred Celsius degrees and Ga^{3+} or Zr^{4+} have no significant effect on the temperature at which the mesostructure collapses.

Keywords: Mesostructured titania; Heteroelements; Crystallization; Phase transformation; Thermal Stability

1. Introduction

Titanium dioxide is widely used in the formulation of sunscreen and plastics, as pigments or in catalysis [1]. It is also a semiconductor widely considered for its photocatalytic properties [2,3]. For example, TiO_2 is a good photocatalyst for wastewater treatment, air purification or self-cleaning surfaces [4-6]. Depending on the targeted application, one of the crystallographic forms of titania should be favored during the titania preparation. Indeed, among the three main polymorphs anatase, rutile and brookite [7], having the TiO_6 octahedron as the common primary structural unit, the photocatalytic activity of TiO_2 is mainly attributed to its anatase phase [8,9], which is the most thermodynamically stable at the nanosized level. The specific surface area is also another crucial parameter that should be taken into account for photocatalysis. Indeed, because a large surface area provides more active sites for adsorbing molecular organic pollutants such as dyes, photocatalysts with large surface area are likely to exhibit better photocatalytic activity. Rutile, the most thermodynamically stable phase in bulk materials, is more desirable for applications in the fields of pigments or lithium ions batteries [10,11].

Moreover, when used as catalyst support, for hydrodesulfurization reaction for example, TiO_2 can lead to quite different catalytic properties (in terms of activity and selectivity) compared to the conventional γ-alumina support [12]. However, TiO_2 is rarely used as a catalyst support mainly because of its low specific surface area (for example ≈ 50 $m^2\ g^{-1}$ for the commercial P25 against 230 $m^2\ g^{-1}$ for γ-Al_2O_3) and thermal stability (anatase phase usually crystallizes from 300°C and the transition from anatase to rutile phase occurs between 500 and 600°C).

The applications of titania in (photo)catalysis thus show the interest to prepare TiO_2 with high specific surface area, thermal stability and to have tools to tune the anatase-rutile transition temperature. One way to reach this goal deals with the dispersion of titania onto another oxide with a high specific surface area such as mesostructured silica or γ-alumina [13-17]. For

example, Chao and coll. [17] have reported that in comparison with bare Al_2O_3, the addition of TiO_2 to alumina support leads to the formation of catalysts, which have higher activities for the hydrodesulfurization of thiophene. Another alternative to increase the specific surface area consists in preparing mesoporous titania. The latter, are usually synthesized from the sol-gel process using titanium alkoxides as precursors. Following this approach, the textural properties of the TiO_2 materials are mainly controlled by the synthesis conditions such as the pH, the gel composition, the humidity and so on [18]. The textural properties of the porous titania can be further enhanced by combining the sol-gel process with the surfactant templating route, reported for the preparation of the ordered mesoporous silica materials. In that case the materials can be prepared according to various pathways [19]. For example, Yamauchi and coll. have developed a new strategy of polymeric micelle assembly for the synthesis of mesoporous materials with large mesopores in the range from 30 to 50 nm using asymmetric triblock copolymers with a long hydrophobic segment and a reactive segment for strong interaction with the inorganic precursor [20,21]. Based on the sol-gel chemistry, Yamauchi and coll. have also prepared antibacterial mesoporous titania films using Pluronic P123 as surfactant and titanium tetraisopropoxide as inorganic precursor. The obtained films show superior antibacterial activity than the commercially or metal doped photocatalysts reported in literature [22]. Among the different pathways, the evaporation-induced self-assembly (EISA) method is one of the most used synthetic methods in the research area of surfactant-assisted mesoporous titania [15,19,23,24]. However, the recovered materials are usually amorphous and in most of the cases the mesostructure collapses and most of the porosity is lost after being heating at 300-350 °C because of the intrinsic crystallization of anatase [25]. Thus, the limitation of the crystallization temperature below 400°C, is far under the required temperature (550°C) to completely transform amorphous TiO_2 into anatase. Because of the important role of titania in (photo)catalysis, as reminded above, up to now

many efforts are still devoted to control the crystallization of the amorphous walls and the anatase to rutile phase transition to get the adequate crystallographic form of titania for the targeted applications. In respect with this objective, Li and coll. [26] have developed a method to control *in situ* the crystallization of mesostructured titania. Their strategy consists in incorporating an amorphous inorganic oxide such as P_2O_5 or SiO_2 into the titania framework. By this way composites in which TiO_2 nanocrystallites are glued by amorphous matrix are prepared. Dong and coll. used this method to synthesize highly ordered 2D hexagonal mesoporous TiO_2/SiO_2 composite with variable Ti/Si ratios by EISA process using titanium isopropoxide and tetraethylorthosilicate as precursors, triblock P123 copolymer as templating agent and a large amount of HCl to control the co-condensation of the precursors [27]. The photocatalytic activities of these composites for the degradation of a large variety of anionic and cationic dyes in aqueous solution were found excellent and higher than those of the commercial TiO_2 P25. It was demonstrated that the surface properties of these TiO_2/SiO_2 nanocomposites can be modulated by varying the Ti/Si ratio and the calcination temperature to adapt them for an optimal adsorption (number of surface hydroxyls) and efficient photodegradation (size and crystallinity of anatase nanocrystals) according to the nature of the dye [28,29]. Another method to increase the thermal stability and to control the anatase to rutile transformation consists in introducing heteroelements such as lanthanides, cerium, aluminum and so on in the titania matrix [30-37]. For example, Shin and coll. [37] have shown that lanthanum-incorporated mesoporous TiO_2 materials have a higher surface area, pore volume and pore diameter than the pure mesoporous TiO_2. In addition, the presence of the lanthanum prevents from the collapse of the mesostructure and the growth of the titania nanocrystallites.

In previous studies, we have reported the synthesis of mesostructured titania with 2D hexagonal porous network, having semi-crystalline framework and with high specific surface

area (> 250 m²/g). Our synthesis strategy combined EISA with the Liquid Crystal Templating (LCT) pathway [38,39]. Pluronic P123, an amphiphilic triblock copolymer, is used as pore templating agent and titanium isopropoxide as inorganic precursor. Using our method, Steinfeldt and coll. [40] have investigated the effect of Fe, Co and Ni addition on the photocatalytic activity of these mesostructured TiO_2. They have shown that after calcination at 450°C, at low content (0.5 mol.%) the presence of the doping metal does not modify the mesopore ordering. An improvement in the phenol degradation compared to the pristine titania is noted when Fe or Co are used as dopants. By contrast, at higher metal content (5 mol.%) the hexagonal structure is maintained only for titania containing Ni and whatever the metal, the phenol degradation is inhibited because of the formation of an Fe, Co or Ni amorphous oxide phase located at the TiO_2 surface.

In the present paper, we have investigated in detail the effect of the introduction of heteroelements (Si, P, Al, Ge, Ga and Zr) on the thermal stability of the semi-crystalline mesostructured titania. The thermal stability will be defined by considering both the temperature at which the mesostructure collapse (noted T_c) and the temperature at which the transition from anatase to rutile occurs (noted T_R).

2. Materials and methods

The triblock copolymer Pluronic P123 $(EO)_{20}(PO)_{70}(EO)_{20}$ (EO = ethylene oxide, PO = propylene oxide) was purchased from Sigma-Aldrich. Titanium isopropoxide $Ti(OiPr)_4$, tetramethylorthosilicate, zirconium propoxide, trisec aluminum butoxide, germanium isopropoxide, gallium (III) nitrate hydrate [$Ga(NO_3)_3$, nH_2O] and phosphoric acid were purchased from Aldrich and used as inorganic source. Hydrochloric acid (ACS reagent, 37%wt, Sigma-Aldrich) was employed to control the rate of hydrolysis of $Ti(OiPr)_4$.

2.1. Materials preparation: Materials have been prepared according to the surfactant templating pathway. First, 1 g of P123 surfactant was dissolved into 20 g of ethanol under stirring at room temperature. Then, 2 g of a hydrochloric acid solution (37 %wt), 3 g of titanium isopropoxide [$Ti(OiPr)_4$] and 2 g of water were added. Afterwards x g of X where X corresponds to Si^{4+}, Zr^{4+}, Al^{3+}, Ge^{4+}, Ga^{3+} and PO_4^{3-} were incorporated. The X content in the mixture was fixed to 10 mol.% compared to Ti^{4+}. The mixture was directly evaporated under vacuum (55 °C, 25 mbar) to remove ethanol and other alcohols released by hydrolysis of the alkoxides. Samples were dried in an oven at 40°C for 12 h. Then they were placed under an atmosphere of NH_3 (≈ 0.5 atm) for 12 h to complete the condensation of the titania precursor [40]. The final products were recovered after surfactant extraction with ethanol (Soxhlet method) during 8 hours. After this step all the materials have an amorphous mesopore framework.

To investigate the effect of X on the thermal stability of the obtained amorphous mesostructured materials, the samples were calcined at different temperatures, from 380 to 900°C under synthetic air atmosphere. They were first heated to 150°C, at a rate of 1 °C / min and kept at this temperature during one hour. Afterwards, the same program was applied to reach the final temperature of 380, 500, 600, 700, 800 or 900°C.

2.2. Characterization:

SAXS experiments were performed on a SAXSess mc² instrument (Anton Paar), using a line collimation system. This instrument is attached to a ID 3003 laboratory X-Ray generator (General Electric) equipped with a sealed X-Ray tube (PANalytical, $\lambda_{Cu,\ K\alpha} = 0.1542$ nm) operating at 40 kV and 50 mA. A multilayer mirror and a block collimator provide a monochromatic primary beam. A translucent beam stop allows the measurement of an attenuated primary beam at q=0. Mesoporous materials or hybrid mesophase were put

between two sheets of Kapton® placed in a powder cell before being introduced inside the evacuated chamber. All data were corrected for the background scattering from the Kapton® and for slit-smearing effects by a desmearing procedure from SAXSQuant software using the Lake method. Powder X-ray diffraction patterns were recorded using a PANalytical X'Pert PRO diffractometer equipped with a Cu X-ray tube ($\lambda_{Cu(K\alpha)} = 0.1542$ nm) operating at 45 kV and 40 mA and a X'Celerator detector. Fixed divergence slit (1/16), mask (10 mm) and antiscatter slit (1/8) were used at primary beam for the current analysis. The phases identification has been realized with the X'Pert Highscore software (PANalytical) and the PDF-4+ database from the International Centre for Diffraction Data (ICDD). The anatase crystallite size was estimated by applying the Scherrer equation using the principal diffraction peak corresponding to the plane (101) of anatase. The Scherrer constant used was $K = 0.9$ and the β instrumental was taken for the FWHM of (101) plane of a micrometric anatase.

Raman Scattering Spectra were collected on a Jobin-Yvon T64000 spectrometer equipped with an optical microscope in confocal mode. The excitation beam (514.5 nm) was focused using a long-frontal x50 objective (numerical aperture 0.5) on an area of about 3 μm^2. The laser power on the sample was approximately 10 mW. The spectral resolution was 3 cm^{-1}, with a wavenumber precision better than 1 cm^{-1}.

Scanning Electron microscopy (SEM) images were recorded with a JEOL JSM-7900F scanning electron microscope (SEM) equipped with a BRUKER QUANTAX spectrometer for the energy dispersive X-ray analyses (EDX).

Transmission Electron Microscopy (TEM) observations were performed using a Jeol ARM-200F microscope working at 200kV. Elemental mappings were done with an EDX Jeol Centurio detector.

N_2 adsorption-desorption isotherms were determined on a Micromeritics TRISTAR 3000 sorptometer at –196 °C. The specific surface area was obtained by using the BET model

whereas the pore diameter and the pore size distribution were determined by the BJH (Barret, Joyner, Halenda) method with KJS (Kruk, Jaroniec, Sayari) correction applied to the adsorption branch [42, 43].

^{1}H decoupled ^{29}Si MAS NMR and ^{1}H-^{29}Si Cross Polarization Magic Angle Spinning (CPMAS) NMR spectra have been recorded at room temperature on a Bruker Avance NEO 300WB spectrometer (B_0=9,4T) operating at B_0 = 7.1 T giving Larmor frequencies of 59.61 MHz for ^{29}Si and 300.08 MHz for ^{1}H. Samples were packed in a 7mm diameter cylindrical zirconia cramps rotor fitted with Kel-f end caps and spun at a spinning frequency of 4 kHz. ^{1}H-^{29}Si CPMAS NMR experiments were performed with a proton $\pi/2$-pulse duration of 5.2 μs, a contact time of 4 ms, and a recycle delay of 3 s. ^{1}H spin lattice relaxation times (T_1) was measured with the inversion-recovery pulse sequence. ^{1}H decoupled ^{29}Si MAS NMR spectra were recorded with a carbon $\pi/6$-pulse duration of 1.7 μs, a recycle delay of 80s and a ^{1}H high-power decoupling of 69 kHz. The number of scans varied from 4500 to 7600 depending on the particular sample. ^{29}Si chemical shifts are reported relative to external Tetramethylsilane (TMS).

^{31}P MAS NMR spectra have been recorded at room temperature on a Bruker Avance NEO 400WB spectrometer (B_0=9,4T) operating at a Larmor frequency of 161.99 MHz. Samples were packed in a 2.5mm diameter cylindrical zirconia rotor fitted with Vespel end caps and spun at a spinning frequency of 30 kHz. ^{31}P MAS NMR experiments were performed with a proton $\pi/2$-pulse duration of 2.0 μs and a recycle delay of 150 s. ^{31}P spin lattice relaxation times (T_1) was measured with the saturation-recovery pulse sequence. The number of accumulations was typically 600. H_3PO_4 (85% in water) was used as external reference.

^{27}Al MAS NMR spectra have been recorded at room temperature on a Bruker Avance AVANCE NEO 400WB spectrometer (B_0=9,4T) operating at 104.23 MHz. Samples were packed in a 2.5mm diameter cylindrical zirconia rotor fitted with Vespel end caps and spun at

a spinning frequency of 25 kHz. ^{27}Al MAS NMR experiments were collected with a proton $\pi/12$-pulse duration of 0.33 µs and a recycle delay of 1 s. The number of accumulations varied from 50000 to 90000. The chemical shifts were referenced to external $[Al(H_2O)_6]^{3+}$ in $AlCl_3$ aqueous solution.

The transmission FTIR spectra were obtained with a resolution of 4 cm^{-1} with a Bruker Equinox IFS 55 spectrophotometer equipped with a DTGS detector. To perform the analysis, the sample powder was first diluted in KBr matrix (1 wt%).

3. Results and discussion

3.1 Structural characterization: The SAXS pattern (Fig. S1) of the extracted TiO_2 is characteristic of a mesostructured titania as reported previously [38,39] and upon calcination the mesostructure begins to collapse at 600°C. Indeed, after treatment at this temperature a large and not well resolved peak is observed on the SAXS pattern. If the calcination is performed above 600°C, no reflection is detected any longer, reflecting the complete collapse of the mesoporous network.

After extraction, all the materials prepared in the presence of heteroelements exhibit similar SAXS patterns than the bare titania. However, we note a shift of the position of the first reflection (10.2 nm for bare TiO_2) towards higher d values for Ge^{4+} (11.2 nm), Al^{3+} (12.9 nm) and Ga^{3+} (11.0 nm) and lower d value for Zr^{4+} (8.4 nm). The position of this peak remains almost unchanged for PO_4^{3-} (10.3 nm) and Si^{4+} (10.1 nm). In addition, incorporating aluminum, it seems that a second component appears at around 9.0 nm.

No line is observed of the SAXS patterns after heating at 900°C for PO_4^{3-}, Al^{3+} and Zr^{4+} or at 700°C for Ge^{4+} and Ga^{3+} (Fig. S1). Concerning TiO_2 containing Si^{4+} a broad peak at lower q with a shoulder indicating a remaining mesostructuration is observed after calcination at 900°C. It is noteworthy that a broad peak more or less intense appeared at low q values for all

samples before losing any mesostructuration (no reflection) on the SAXS patterns of all materials. This peak is assumed to reflect the presence of anatase nanoparticles homogeneous in size and thus with a more or less regular interparticular distance, and also to indicate the collapse of the mesostructure. Considering that the collapse of the mesostructure has occurred at the temperature for which this peak is observed (Fig. S1), the effect of the presence of heteroelement on the collapse temperature (T_C) of the mesostructured TiO_2 can be ranked in the following order: Si^{4+}, PO_4^{3-} (800°C) > Al^{3+}, Ge^{4+} (700°C) > Ga^{3+}, Zr^{4+} (600°C; value corresponding to the one of the bare TiO_2) (Table 1). After calcination at 800°C, the correlation distance corresponding to this peak is 25.3, 35.0 and 28.5 nm for PO_4^{3-}, Al^{3+} and Zr^{4+}, respectively. We can note that the correlation distance increases as a function of calcination temperature for Al^{3+} and Zr^{4+}. For instance, it varies from 17.1 to 35.0 nm, when TiO_2 containing Al^{3+} is heating from 700 to 800°C and from 19.0 to 28.5 nm when TiO_2 containing Zr^{4+} is heating from 600 to 800°C (Fig. S1).

Comparing with the corresponding extracted material, whatever the added heteroelement, after calcination a shift of the first reflection towards lower d value is observed. For example, it varies from 10.2 to 8.9 nm and 8.4 nm after heating the bare mesostructured titania at 380°C and 500°C, respectively. This phenomenon can be attributed to a condensation of the Ti-OH groups but also to the crystallization of the walls. Indeed, after heating the bare mesostructured TiO_2 at 380°C mainly amorphous phase is obtained and after calcination at 500°C the peaks at 2θ = 25.35 (101), 38.30 (103) (004) (112), 48.10 (200), 54.01 (105), 55.09 (211) and 63.23° (204) reveal clearly the presence of anatase (Fig. S2). These peaks are quite broad, reflecting the formation of nanosized anatase. Increasing the heating temperature, the diffraction peaks become narrower, more intense and better resolved, indicating the enhancement of the crystallization degree and/or the growth of the particles. It is noteworthy, that a low intense and broad peak is observed at around 2θ = 25.4° for bare TiO_2 calcined at

380°C indicating the formation of anatase nanocrystallites. After heating at 700°C, traces of rutile are detected and after heating at 900°C the signature of the rutile polymorph is clearly observed at 2θ = 27.51 (110), 36.13 (101), 41.30 (111), 54.38 (211) and 56.70° (220). In the presence of heteroelements, the same evolution is observed but with shifts in the temperatures at which the nanosized anatase and the rutile phase appear (Table 1). The phase β–TiO_2, which adopts a cubic structure such as anatase but with oxygen deficiencies can also coexist with the nanosized anatase and it is transformed into anatase when the heating temperature is raised (Fig. S2). It should be highlighted that no rutile is detected by XRD when PO_4^{3-} or Si^{4+} are incorporated into the mesostructured titania. The size of anatase particles has been determined with the Scherrer equation (Table 2). From Tables 1 and 2, one can find a good correlation between T_C and the size of the anatase particles. Indeed, the collapse of the mesostructure seems to occur when the anatase particle size exceeds 10 nm (except for bare TiO_2 and TiO_2 containing Si^{4+} for which the collapse occurred for an average particle size of 18 and 8 nm, respectively). The collapse of the mesostructure can therefore be mainly related to the transformation of nanosized anatase into bulk anatase. A plot of the anatase particle size versus the correlation distance corresponding to the broad SAXS peak observed at low q shows a linear dependence that confirms its attribution to the presence of nanoparticles homogeneous in size (Fig. 1). X-ray diffractograms of titania containing PO_4^{3-}, Ga^{3+} and Zr^{4+} also show the presence of TiP_2O_7, Ga_2O_3 and brookite or Ti_2ZrO_6 after heating at 900°C, respectively. For TiO_2 containing Zr^{4+}, the position of the (100) anatase reflection as well as the position of the other reflections are slightly shifted to lower 2θ and their position correspond to an anatase phase incorporating 10 mol.% Zr ($Zr_{0.1}Ti_{0.9}O_2$, ICDD card n° 04-013-9937). Depending on the heating temperature and on the heteroelement, the presence of the various titania polymorphs is also supported by the Raman analysis (Fig. S3). Indeed, in the literature it is reported that the peaks in the range 200-800 cm^{-1}, are characteristic of Ti-O-

Ti network and are generally observed in all the forms of TiO_2 [44]. The presence of an intense peak around 140 cm^{-1} is characteristic of the anatase crystalline TiO_2 [45]. On the Raman spectrum depicted in Figure 4, the bands at 141, 194, 393, 514 and 639 cm^{-1}, for the bare TiO_2, are attributed to the E_g, B_{1g}, A_{1g} or B_{1g}, and E_g modes of anatase, respectively [46]. After heating at 800°C, besides the vibration of anatase the combination band, the E_g and A_{1g} of rutile [47] appear at around 229, 445 and 605 cm^{-1} (Fig. S3), respectively. In a general way there is a good accordance between the Raman and the XRD results (Table 1). However, slight differences can be noted concerning the temperature at which the nanosized anatase and/or the rutile phases appear. This can be explained by the fact that Raman spectroscopy is a more sensitive technique for the detection of nanosized crystalline domains [48]. Moreover, when anatase is present, its signature is exalted and because of the anatase modes are relatively dominant, it is hard to observe the vibrations characteristic of the other phases such as rutile.

SEM and TEM observations with EDX analysis have been realized on materials calcined at 380°C and at the temperature at which the peak due to the presence of particles clearly appear on SAXS patterns (Fig. 2). SEM and TEM images confirm the mesostructuration of all materials thermally treated at 380°C (Fig. 2: 1st and 2nd columns). From TEM images it appears that the mesostructure differs depending on the nature of the heteroelement (Fig. 2: 2nd column). The incorporation of Si^{4+} has led to a more ordered mesostructure. It can be observed in some areas some parallel fringes reflecting the presence of linear channels and their hexagonal packing such as expected for 2D hexagonal mesostructure. The incorporation of Zr^{4+} and Ga^{3+} has led to smaller pores, and with thicker walls in the case of Ga^{3+}. Concerning the incorporation of Al^{3+}, Ge^{4+} and PO_4^{3-}, mesopores appears larger with thin walls. Some channels aligned forming some ordered mesostructures are observed by SEM for TiO_2 containing Ge^{4+}. When materials are calcined at higher temperatures both SEM and

TEM observations reveal for all the presence of nanoparticles relatively homogeneous in size and show the presence of interparticle porosity (Fig. 2: 3rd and 4th columns). The formation of these nanoparticles is in agreement with SAXS and XRD results and are mainly anatase. For TiO_2 containing Si^{4+} calcined at 800°C, the particles are much smaller than for bare TiO_2 calcined at 600°C, TiO_2 containing PO_4^{3-} calcined at 800°C and TiO_2 containing Al^{3+}, Ge^{4+}, Ga^{3+} or Zr^{4+} calcined at 700°C. Although the determination of the particle size by TEM is difficult because particles are highly aggregated and overlap. Moreover, some other crystalline phases such as rutile (Ti-Ge calcined at 700°C), β-TiO_2 (TiSi and TiP calcined at 800°C) and Ti_2ZrO_6 or Brookite (TiZr calcined at 700°C) are coexisting with anatase particles. However, the particle sizes have been determined from the TEM images (from an average of about 20 measurements) and are reported in the Table 2 (values in brackets). They are in good agreement, except for TiGe and TiGa, with the size determined from XRD patterns (Scherrer equation) although this latter concerns only anatase particles. For TiGe and TiGa the difference is probably due the higher polydispersity of the particle size. EDX analyses were done with both SEM and TEM techniques on TiO_2 containing heteroelements (Fig. S4 and S5, respectively). These analyses allowed to characterize the heteroelement dispersion at two different scales. EDX element mappings recorded with SEM on materials calcined at 380°C show that heteroelements are homogeneously dispersed except Al^{3+} and Ga^{3+} for which some area rich or poor in Al and Ga, respectively, are present (Fig. S4). The incorporation of the heteroelement Ga appears particularly heterogeneous. After treatment at higher temperature, heterogeneities in the dispersion of the heteroelement were still observed for Al^{3+} and Ga^{3+} but also for Ge^{4+}. EDX element mappings recorded with TEM reveal a homogeneous dispersion of all heteroelements after thermal treatment at 380°C and at higher temperatures (800°C for Si^{4+} and PO_4^{3-}, and 700°C for Al^{3+}, Ge^{4+}, Ga^{3+} and Zr^{4+}). EDX element mappings were also recorded from SEM and TEM for TiO_2 containing Zr calcined at

900°C and revealed a homogeneous dispersion of Zr (Fig. S6). The fact that Zr appears homogeneously dispersed could indicate that the crystalline phase observed by XRD and coexisting with anatase and rutile phases on TiO_2 containing Zr calcined at 900°C is Ti_2ZrO_6.

3.2. Textural properties: Below T_C, whatever the sample, a type IV isotherm with H2 hysteresis loop, characteristic of mesoporous materials according to the IUPAC classification [49] is obtained by manometry nitrogen adsorption/desorption (Fig. S7). The total pore volume determined at high relative pressure p/p_0 = 0.99 (a lower p/p_0 is used for determination of total pore volume when there is a weak increase of adsorbed volume due to large interparticular mesopores such as it is the case for bare TiO_2 and Ga^{3+}) decreases progressively with the increase of the calcination temperature (Fig. 3A). For example, for titania containing Si^{4+}, the pore volume value drops from 0.55 to 0.22 cm³/g-STP if the heating temperature is varied from 380 to 800°C (T_C value for TiO_2 containing Si^{4+}). Likewise, the specific surface area determined by the BET method is strongly affected by the increase of the thermal treatment temperature (Fig. 3B). Depending on the nature of the heteroelement added, at the temperature of the mesostructure collapse (T_C), the specific surface maintains between 41 and 57% of the value determined for the corresponding extracted titania-based material. The pore volume at T_C represents between 40 and 55% of its initial values. It is noteworthy that both, total pore volume and specific surface area, are of the same order of magnitude for all materials except for TiO_2 containing Ga^{3+}, which are lower. This may be related to the heterogeneous incorporation of Ga observed by EDX-SEM. Indeed, the presence of non-porous Ga rich phases could explain the lower textural characteristics of the TiGa material that includes both mesoporous TiO_2 rich phases and non-porous Ga rich phases.

Regarding the textural properties, the mesostructured titania prepared in the presence of 10 mol.% of Si^{4+} have a higher thermal stability than the one of the 15Si-Ti obtained through an aqueous sol-gel method in the absence of surfactant by the addition of 15 mol.% of silica [50]. Indeed, after calcination at 500°C the specific surface area and the pore volume are 310 m²/g and 0.49 cm^3/g against 187 m²/g and 0.17 cm^3/g for the 15Si-Ti. After heating at 800°C, the mesostructured titania containing Si^{4+} still exhibits higher specific surface area and pore volume than the 15Si-Ti (176 m²/g against 93 m²/g and 0.22 cm^3/g against 0.11 cm^3/g).

Below Tc, in function of the calcination temperature, the inflection due to capillary condensation moves toward smaller values of relative pressure. Since the p/p_0 position of the inflection point is related to the pore diameter by the Kelvin's equation, it can be inferred that a decrease of the mean pore diameter occurs when the heating temperature is raised. This is confirmed by the mesopore size distributions depicted in Figure 8. Indeed, at least a maximum, which is shifted towards lower values when the calcination temperature is progressively increased until T_C, is present. For example, for TiO_2 containing Si^{4+}, the mesopore diameter varies from 6.3 to 5.6 nm if the heating temperature is increased from 380 to 800°C (Fig. 4 and Table 3). When Al^{3+} or PO_4^{3-} are incorporating during the synthesis of titania two components with very close maxima are even detected (Fig. 4 and Table 3). However, it should be noted that even if two mesopores sizes are observed since their values are close to each other, the isotherms present only one inflection point related to the capillary condensation step (Fig. S7). In the case of aluminum, correlating this observation with the fact that two components are also detected on the SAXS patterns (at 12.9 and 9.0 nm for the extracted material), we can assume that two mesopores networks coexist for titania prepared in the presence of Al^{3+}. Taking into account the error on the measurement, up to T_C TiO_2 containing Si^{4+}, Ge^{4+} and Ga^{3+} have mesopore diameters in the same range of order than the

bare titania but they exhibit broader pore size distribution. In the opposite, addition of Zr^{4+} leads to materials with smaller mesopores (Fig. 4 and Table 3).

Above Tc, the isotherms bare TiO_2, Ge^{4+} and Ga^{3+} evolve from type IV isotherms with a H3 hysteresis loop to flat or type II isotherms. Meantime, the mesopore size distribution is flat (Fig. 4) indicating that there is almost no mesoporosity detectable by the technique. However, type IV isotherms with a H3 hysteresis loop are still observed for Si^{4+}, Zr^{4+} and Al^{3+}. It is also interesting to note that for TiO_2 containing PO_4^{3-}, Al^{3+}, Ge^{4+}, Ga^{3+} or Zr^{4+} the mean pore size decreases until the Tc and increases after heating at higher temperatures. For Zr^{4+} and Al^{3+} materials it is also clearly observed above Tc a broad SAXS peak at low q that is shifted to lower q and the mesopore size distributions become very broad with the increase of the calcination temperature. These results confirm that broad peaks at low q on SAXS patterns are due to nanoparticles that generate interparticle pores.

Moreover, it is in accordance with the collapse of the mesostructure. Much higher mean mesopore diameters than those determined at T_C are observed. For example, for TiO_2 containing Zr^{4+}, the pore size increases from 6.5 nm at T_C to 15.1 nm after heating at 800°C. The values reported in Table 3 are not compatible with surfactant templated mesopores but they are likely due to particles arising from the collapse of the network. This hypothesis is supported by the SAXS analysis with the presence of a broad peak at low q whose correlation distance increases with heating temperature (Fig. S1). In all cases, the collapse of the mesostructure and the formation of nanoparticles have been confirmed by SEM and TEM observations. For titania containing Si^{4+} after calcination at 800°C and 900°C the nanoparticles were found much smaller (Table 2) that can explain that after calcination at 900°C the specific surface still reached 124 m²/g against 9, 18, 3 and 24 m²/g for TiO_2 containing Ge^{4+}, Al^{3+}, Ga^{3+} and Zr^{4+}, respectively.

3.3. Study of the heteroelement environment: Solid state NMR experiments were run to investigate the evolution of the environment of the heteroatoms with the increase of the heating temperature when it was possible such as for TiO_2 containing PO_4^{3-}, Si^{4+} and Al^{3+} materials. TiO_2 containing PO_4^{3-} calcined at 380, 600, 800 and 900°C have been analyzed by ^{31}P MAS NMR (Fig. 5A). For materials calcined at 380, 600 and 800°C broad resonances are observed. The spectra were fitted with DMFit software [51] with 5 resonances at about 1.3, -5.1, -11.3, -16.7 and -28.4 ppm. Studies of amorphous or crystalline titanium phosphates have shown a correlation between connectivity and chemical shift [52,53]. As the connectivity increases, an upfield shift is observed. The weak resonance at about 1.3 ppm is characteristic of H_3PO_4 most probably adsorbed on the material surface. The other four resonances at about -5.1, -11.3, -16.7 and -28.4 ppm were attributed to H_2PO_4 with 1P-O-Ti bound (monodendate structure $Ti(H_2PO_4)_4$), HPO_4 with 2 P-O-Ti bounds (bidentate structure $Ti(HPO_4)_2$), HPO_4 or PO_4 with 3 P-O-Ti bounds (such as in a-$Ti(PO_4)_2$-H_2O) and PO_4 with 4P-O-Ti bounds (such as in $NaTi_2(PO_4)_3$), respectively [52,53]. After calcination at 380°C, the ^{31}P MAS spectrum exhibit two main resonances at -5 and -10.5 ppm in agreement with the major presence of monodentate and bidentate titanium phosphate structures. The major presence of monodentate species indicate that phosphate species exist as Ti-O-P in the bulk TiO_2. At higher temperature the proportion of monodentate species decreases and the one of bidentate species increases indicating the condensation of H-containing groups. When thermally treated at 600°C, three main resonances at about -5, -12 and -15.8 ppm are observed indicating that monodentate and bidentate titanium phosphate structures are still present but structures with 3 P-O-Ti bonds have been formed. After thermal treatment at 800°C, the main resonances appear at -10.3, -17.6 and -28.4 ppm: the monodentate titanium phosphate structures have disappeared and structures with 4 P-O-Ti bonds have been formed. The formation of structures with 3 and 4 P-O-Ti bonds indicate the dehydration of adjacent P-OH groups.

These results clearly indicate that the connectivity increases with the temperature of the thermal treatment. The concentration of P increases locally, probably around TiO_2 anatase nanocrystallites and slow down their growth. The spectrum of TiO_2 containing PO_4^{3-} calcined at 900°C is very different and displays several thin resonances from -39.4 to -52.5 ppm that are characteristic of crystalline TiP_2O_7 those presence was also observed by XRD. Weak resonances are also observed between 0 and -30 ppm indicating the residual presence of amorphous titanium phosphate species. A weak thin resonance is also observed at -28 ppm that was attributed to an unknown titanium crystalline phase [53]. The relative proportion of the crystalline phase TiP_2O_7 in which 1 phosphorus is coordinated via 3 oxygen to 3 titanium is about 80%. These ^{31}P MAS NMR results are consistent with FTIR data (Fig S8a). Indeed, a broad band at 1074 cm^{-1} attributed to $H_2PO_4^{2-}$ [54,55] is observed for material calcined at 380°C, it shifts to 1109 cm^{-1} after calcination at 600°C and splits into two bands at 1034 cm^{-1} and 1205 cm^{-1} after calcination at 800°C. The band at 1034 cm^{-1} was attributed to Ti-O-P bond [53]. After thermal treatment at 900°C the FTIR spectrum displayed the bands at 960, 979, 1049, 1092, 1205 et 1281 cm^{-1} that are characteristics of the $P_2O_7^{4-}$ from TiP_2O_7 phase [53]. At 900°C the mesostructure has totally collapsed, the N_2 physisorption isotherm is flat and particle size has strongly increased (83 nm at 900°C against 16 nm at 800°C): it is assumed that amorphous titanium phosphate species (structures with 3 and 4 P-O-Ti bonds) that surrounded the TiO_2 anatase have crystallized in TiP_2O_7 and thus the glue effect was no more effective.

The TiO_2 containing Si^{4+} materials calcined at 380, 600 and 800°C were analyzed by ^{29}Si NMR using MAS+DEC and CP-MAS techniques. Due to the low natural abundance of the ^{29}Si nucleus, the long spin–lattice relaxation time T1 and the low amount of Si in the samples (10 mol.% or 3.3 wt.%) the resulting ^{29}Si MAS+ DEC NMR spectra (Fig. S9) have very low resolution although a long acquisition time (from 4 to 7 days). Nevertheless, four resonances

at -82, -90, -99 and -108 ppm that correspond to Q^1 ($(HO)_3$-Si(OX…), Q^2 ($(HO)_2$-Si(OX…)$_2$), Q^3 (HO-Si(OX…)$_3$ and Q^4 (Si(OX…)$_4$) units (X = Si or Ti), respectively are observed (Fig. S9). According to Okada and coll. [56] the presence of four-coordinated Si species excludes the incorporation of Si into anatase structure. Although the cross-polarization ^{1}H-^{29}Si MAS NMR technique is not quantitative if surrounding protons are of different nature and/or not at the same distance from the Si atoms, ^{29}Si CP-MAS spectra have been also recorded and they confirmed the presence and the position of the Q^n units (Fig. 5B). From both ^{29}Si MAS and CP-MAS experiments it can be concluded that both samples calcined at 380 and 600°C contain mainly Q^1, Q^2 and Q^3 units with a lower ratio $Q^3/(Q^1+Q^2)$ for the one calcined at 380°C, which indicate a lower degree of condensation than the one calcined at 600°C. The sample calcined at 800°C present almost no Q^1 units, a major contribution of Q^3 and a more noticeable contribution of fully condensed Q^4 units. These results indicate an increase of the condensation of the silica network when calcination temperature increases as previously reported in the literature for TiO_2 containing SiO_2 xerogels [56,57]. This is in agreement with FTIR data, which showed a low intense band at 1013 cm^{-1} attributed to Si-O-Si bond whose intensity increased and position shifted to 1075 cm^{-1} when temperature increased to 800°C (Fig. S8b). A band at 914 cm^{-1} characteristics of Si-O-Ti bond is also observed and shifted to 937 cm^{-1} without noticeable increase of its intensity when calcination temperature increased from 380 to 800°C. Both ^{29}Si NMR and FTIR data suggest that Ti-O-Si bonds are formed and dissociate under thermal treatment at high temperature to form Si-O-Si bonds. This is in agreement with the occurrence of a micro phase separation that result in the formation of a SiO_2 layer on the TiO_2 particles surface [27]. This SiO_2 layer would inhibit the anatase crystallization and thus would induce a delay in the anatase to rutile transition.

The Al^{3+} containing TiO_2 materials have been analyzed by ^{27}Al MAS NMR (Fig. 5C). After heating at 380°C three main broad resonances are observed at 53, 28 and 0 ppm, which

correspond to tetrahedral, pentacoordinated and octahedral Al atoms [58]. The positions of the 2 resonances attributed to tetrahedral and pentacoordinated Al atoms are down shielded and their relative proportions to the one of octahedral Al atoms decrease when the calcination temperature increases. The pentacoordinated Al species that characterize the presence of disordered alumina have almost disappeared at 800°C. The resonance attributed to octahedral Al atoms became thinner after thermal treatment above 500°C and was down shielded to 12.6 ppm after calcination at 900°C, indicating the formation of a transition alumina phase such as corundum α-Al_2O_3. Indeed, a close look at the XRD pattern has revealed the presence of very weak peaks that correspond to α-Al_2O_3 (Fig. S10). After heat treatment at 600°C a thin resonance appeared at 0 ppm and remained until 900°C. It was attributed to the formation of a boehmite-like layer adsorbed on the TiO_2 surface formed by dehydration of $Al(H_2O)_6^{2+}$ species [59] or to the formation of crystalline tielite Al_2TiO_5 phase [60].

3.4. Discussion: Comparing the thermal stability of the titania prepared in the presence and in the absence of heteroelement it is obvious that the most beneficial effect is obtained with Si^{4+} and PO_4^{3-} since no rutile was observed after calcination at 900°C. Al^{3+}, Ga^{3+} and Zr^{4+} enhance the thermal stability by about a hundred degrees (apparition of rutile after treatment at 800°C) but Ga^{3+} and Zr^{4+} has no significant effect on the temperature at which the mesostructure collapses (Tc = 600°C). A peculiar behavior is noted for TiO_2 containing Ge^{4+} since it behaves similarly to the bare titania: rutile was observed from 700°C. This suggests that even at a loading of 10 mol%, Ge^{4+} which have an ionic radius of 0.53 Å [61] completely substitute Ti^{4+} (ionic radius = 0.61 Å). This assumption is first supported by the fact that even after calcination at 900°C, no crystalline form of GeO_2, which crystallizes into a hexagonal structure at 450°C, is detected by XRD and Raman analysis. It is also strengthened by the results reported by Kitiyanan and coll. [62], who in a paper dealing with the preparation of

TiO_2-GeO_2 composites by combining the sol-gel route with a surfactant assisted mechanism, have shown that until 10 mol.%, Ge^{4+} can substitute Ti^{4+}. Above 10 mol.%, all the germanium may not enter the TiO_2 lattice and is present as amorphous GeO_2.

To explain the enhancement of the thermal stability of TiO_2 in presence of PO_4^{3-}, Si^{4+}, Al^{3+}, Zr^{4+} and Ga^{3+}, we have to consider the « glass » theory developed by Li and coll. [26]. In such approach to limit the growth of the titania particles, and therefore prevent the mesostructure collapse, an amorphous component designated as « glass », which acts as a glue for titania nanocrystals, is added to the mesostructured framework either directly as an amorphous component such as P_2O_5 [26] or by co-assembly with the amphiphiles molecules and the titania precursor [63]. During the calcination step, TiO_2 forms anatase nanocrystallites. The walls of the obtained material are thus constituted by the amorphous phase containing heteroelements and the anatase nanocrystallites. The amorphous phase acts as a binder between the anatase nanocrystallites limiting their growth and by this way it prevents the collapse of the mesopore framework. Using a similar strategy Zhou and coll. [64] have synthesized highly crystalline mesoporous TiO_2 materials using a combined EISA-ethylenediamine (EN) approach, where the role of EN is to protect and envelop the hybrid mesophase formed during the process. EN is introduced after the aging process under reflux. It interacts with the formed primary TiO_2 particles and is an effective protector to inhibit their growth and consequently the transformation into an undesired TiO_2 phase. The mesostructure obtained is ordered and stable up to 700 ° C.

Here, when the synthesis of the mesostructured TiO_2 is made in the presence of phosphoric acid, the incorporation of some phosphorous into the titania mesoporous framework as reported by Yu and coll. [65] was evidenced by ^{31}P MAS NMR and FTIR. The walls of the recovered materials are thus constituted of amorphous titanium phosphate and nanosized anatase. The presence of the amorphous titanium phosphate prevents the mesostructure

collapse and delay the anatase to rutile transition through the « glass » effect. In the literature [66] it is also reported that at high temperatures H_3PO_4 can also polymerize to polyphosphoric acid with network structure, which can also participate to the « glass » effect. Moreover, the pore size distribution of the extracted materials presents two components while the SAXS pattern show only one mesopore network, we can thus assume that another part of phosphorous is present in the material as PO_4^{3-} located inside the mesopores and that they partially block them. The formation of TiP_2O_7 after heating at 900°C also suggests that, as reported by Hassan et al for phosphate tin oxide [67], some phosphate groups are adsorbed at the surface of TiO_2 forming amorphous $Ti(HPO_4)_2$. After calcination the dehydroxylation of $Ti(HPO_4)_2$ lead to TiP_2O_7. Nevertheless, the presence of the PO_4^{3-} also contribute to enhance the thermal stability of the mesostructured titania through bond strengthening [68].

The ionic radii of Si^{4+} (0.40 Å), Al^{3+} (0.54 Å) and Ga^{3+} (0.62 Å) [61] are also compatible with at least a partial substitution of Ti^{4+} (0.61 Å) by these cations. The substitution of Ti^{4+} by Al^{3+} lead to oxygen deficiency, which should favor the anatase to rutile transformation [69,70]. Since the opposite trend is observed for the mesostructured titania containing Al^{3+}, as observed by Huang ~~et~~ and coll. [71] in a study concerning the sol-gel synthesis of porous TiO_2 containing Al, we can assume that the substitution is not total and that Al also exist as amorphous Al_2O_3. The presence of amorphous Al_2O_3 was confirmed by ^{27}Al MAS NMR. This amorphous alumina network can arise from the interaction of the alumina precursor with Pluronic P123 and it can be at the origin of the second mesopores network observed by SAXS and manometry nitrogen adsorption/desorption. The ^{27}Al MAS NMR showed that tielite Al_2TiO_5 or a boehmite-like layer was formed on the titania surface after heating at 600°C. But their contribution is minor and the amorphous alumina remains major. The crystallization of a part of amorphous alumina in α-Al_2O_3 after thermal treatment at 900°C was also evidenced by XRD and ^{27}Al MAS NMR. However, it is assumed that the anatase was stabilized by the

amorphous alumina through a moderate « glass » effect since rutile was detected at 800°C against 700°C for the bare TiO_2.

In a similar way, the ionic radius of Ga^{3+} (0.62 Å), which is comparable to the one of Ti^{4+} (0.61 Å) is favorable for the substitutional introduction of Ga^{3+} in the titania framework. However, incorporation of Ga^{3+} introduces into the lattice charge imbalance, which can be compensated by the creation of oxygen vacancies and thus favoring the anatase to rutile transition [72]. However, XRD and Raman spectroscopy show a shift of the transition temperature to a higher temperature region for the mesostructured TiO_2 containing Ga^{3+}. The latter can be attributed to the « glass » effect induced by the presence of amorphous Ga_2O_3, which arise from an excess of gallium. Indeed, even if Ga^{3+} and Ti^{4+} have similar ionic radii, at a loading of 10 mol.%, the substitution of Ti^{4+} by Ga^{3+} is likely incomplete. In paper dealing with preparation of gallium-doped titania nanoparticles, Luo and coll. [73] conclude that until 6.25 at.%, Ga^{3+} could replace Ti^{4+}. Above this content, the substitutional incorporation is saturated and ultra-small gallium oxide clusters are formed on the titania surface. The presence of amorphous Ga_2O_3 is also claimed by Štengl and coll. [74] for amounts of Ga^{3+} in the TiO_2 matrix higher that 2.18 wt.%. For the mesostructured titania containing Ga^{3+}, the presence of amorphous Ga_2O_3 is supported by the fact that heterogeneities in the dispersion of Ga was clearly evidenced by SEM-EDX and that crystalline Ga_2O_3 is detected only after heating at 900°C, temperature at which rutile is observed. The crystallization and/or growth of Ga_2O_3 anneals the « glass » effect.

The enhancement of the thermal stability of the mesostructured TiO_2 containing Si^{4+} can be mainly attributed to the « glass » effect involved by the presence of the amorphous SiO_2 as observed in literature [27,28], even if regarding its size Si^{4+} (0.40 Å) can partially substitute Ti^{4+}. This is confirmed by ^{29}Si NMR and FTIR that clearly evidenced the formation of condensed SiO_2 network when calcination temperature was increased.

Finally, doping mesostructured titania with Zr^{4+}, since the ionic radius of Zr^{4+} (0.72 Å) is a beat higher than the one of Ti^{4+} and lower than the one of O^{2-} (1.40 Å), it can be introduced substitutionally into the matrix, producing some deformation of the lattice [69]. The deformation energy shifts the anatase-to-rutile transition temperature to a higher temperature region [75]. Moreover, the substitution of Ti^{4+} by Zr^{4+} involves a contraction of the mesopore network. This phenomenon was also observed by Zhou and coll., who have reported the preparation of mesoporous composites with high photocatalytic activity and hydrophobicity [76]. When the calcination temperature is increased the crystallinity increased too, involving the collapse of the mesostructure between 500 and 600°C. Because of the big difference in ionic radii between the two cations, Yan and coll. have estimated that the solubility of ZrO_2 in anatase is limited to a Zr/Ti molar ratio of 0.075 [75]. Yu and coll. [77] have investigated $Ti_{1-x}Zr_xO_2$ anatase solid solutions for the photocatalytic degradation of acetone in air and they have shown that some zirconium atoms fail to enter into the titania lattice. In the case of mesostructured titania doped with Zr^{4+}, we can assume that such situation also occurs and amorphous zirconia can thus be formed between the mesostructured titania particles whose thermal stability can be slightly enhanced thanks to the glass effect. After heating at 700°C, the extra amorphous ZrO_2 begins to crystallize as Ti_2ZrO_6 phase.

4. Conclusions

Mesostructured TiO_2 containing heteroelement with enhanced thermal stability have been prepared by combining the sol-gel and the surfactant templating processes. Results show that, thanks to the protector role played by the amorphous oxide such as SiO_2 or Al_2O_3 surrounding the titania crystallites and by comparison with the bare mesostructured titania, the crystallization occurs at higher temperature and the growth of the anatase particles is limited thanks to the « glass » effect. The transformation from anatase to rutile also occurs but at

higher temperature. The efficiency of the heteroelement on the enhancement of the thermal stability can be ranked as follow: Si^{4+} and PO_4^{3-} > Al^{3+} and Zr^{4+} > Ga^{3+} and Ge^{4+}. However, when the crystallites reach the limit size of about 10 nm, the collapse of the mesostructure occurs. Increasing further the calcination temperature titania particles become bigger and bigger, the transition from anatase to rutile takes place and the amorphous heteroelement can also crystallize.

In future work the methodology will be extended to other oxides such as alumina, which also play a key role in catalysis. The developed materials will be used as catalysts and/or catalyst supports for hydrodesulfurization of gazole and/or for the oxidation of volatile organic compounds. Some studies dealing with these topics are already under investigation. Since the temperature of the transition from anatase to rutile is shifted to higher temperature the mesostructured TiO_2 containing heteroelements are also good candidates to be used as photocatalysts.

Conflicts of interest

The authors declare that they have no competing interests

Author Contributions:

Florian Jonas : Investigation
Bénédicte Lebeau : Writing - Original Draft, Supervision
Laure Michelin : Investigation
Ludovic Josien : Investigation
Loïc Vidal : Formal analysis
Cédric Carteret : Resources, Formal analysis
Severine Rigolet : Investigation
Pierrick Gaudin : Visualization
Jean-Luc Blin : Writing - Original Draft, Supervision

Acknowledgments

We would like to thank the platform “Spectroscopies et Microscopies des Interfaces” from LCPME. The platforms “X-ray Diffraction, FTIR and Raman spectroscopy, Electronic Microscopy, NMR” of IS2M are also acknowledged. Florian Jonas thanks the « Region Grand-Est » for the financial support of his PhD.

Funding:

This work was supported by the « Region Grand-Est » [grant number RPHPHXAS-D-AOT17-TITAN].

Appendix A. Supplementary data

Mesopore size distribution obtained from the KJS method applied to the desorption branch of the isotherm (Table S1).

Evolution of the SAXS pattern as a function of the heating temperature of mesostructured titania prepared without and in the presence of heteroelement (S1).

Evolution of the X-Ray diffractograms as a function of the heating temperature of mesostructured titania prepared without and in the presence of heteroelement (S2).

Evolution of the Raman spectra as a function of the heating temperature of mesostructured titania prepared without and in the presence of heteroelement (S3).

SEM images and elemental (Ti and X) mappings of TiO_2 containing heteroelements (S4).

TEM images and elemental (Ti and X) mappings of TiO_2 containing heteroelements (S5).

A) SEM image with C, O, Ti, Zr elemental mappings and B) TEM image with Ti, Zr elemental mappings of TiO_2 containing Zr^{4+} (S6).

Nitrogen adsorption-desorption isotherms as a function of the heating temperature of mesostructured titania prepared without and in the presence of heteroelement (S7).

FTIR spectra (S8).

^{29}Si MAS NMR of TiO_2 containing Si^{4+} (S9).

XRD pattern of TiO_2 containing Al^{3+} calcined at 900°C in the 30-60° 2θ range (S10).

References

[1] O. Carp, C. L. Huisman, A. Reller, Photoinduced reactivity of titanium dioxide, Prog. Solid State Chem. 32 (2004) 33-177.

[2] M. Fox, M. Dulay, Heterogeneous Photocatalysis, Chem. Rev., 1993, 93, 341-357.

[3] M. Pelaez, N. T. Nolan, S. C. Pillai, M. K. Seery, P. Falaras, A. G. Kontos, P. S. M. Dunlop, J. W. J. Hamilton, J. A. Byrne, K. O'Shea, M. H. Entezari, D. D. Dionysiou, A review on the visible light active titanium dioxide photocatalysts for environmental applications, Appl. Catal. B Environ. 125 (2012) 331-349.

[4] M. Hoffmann, M. S. Martin, W. Choi, D. Bahnemann, Environmental Applications of Semiconductor Photocatalysis, Chem. Rev. 95 (1995) 69-96.

[5] U. I. Gaya, A. H. Abdullah, Heterogeneous photocatalytic degradation of organic contaminants over titanium dioxide: A review of fundamentals, progress and problems, J. Photochem. Photobiol. C 9 (2008) 1-12.

[6] B. Lebeau, F. Jonas, P. Gaudin, M. Bonne, J.L. Blin, Dyes depollution of water using porous TiO_2-based photocatalysts, in: N. Dasgupta, S. Ranjan, E. Lichtfouse (Eds.), Environmental nanotechnology, Springer Nature, Switzerland, 2020, pp. 35-92.

[7] A. Linsebigler, G. Lu, J. Yates, J. Photocatalysis on TiO_2 Surfaces: Principles, Mechanisms, and Selected Results, Chem. Rev. 95 (1995) 735-758.

[8] E. Pelizzetti, C. Minero, E.Borgarello, L. Tinucci, N. Serpone, Photocatalytic activity and selectivity of titania colloids and particles prepared by the sol-gel technique: photooxidation of phenol and atrazine, Langmuir 13 (1993), 2995-3001.

[9] B. Ohtani, Y. Ogawa, S. Nishimoto, Photocatalytic activity of amorphous-anatase mixture of titanium(IV) oxide particles suspended in aqueous solutions, J. Phys. Chem. B 101 (1997) 3746-3752.

[10] Q. Gao, X. Wu, Y. Fan, X. Zhou, Low temperature synthesis and characterization of rutile TiO_2-coated mica-titania pigments, Dyes Pigm. 95 (2012) 534-539.

[11] Y. Gan, L. Zhu, H. Qin, Y. Xia, H. Xiao, L. Xu, L. Ruan, C. Liang, X. Tao, H. Huang, W. Zhang, Hybrid nanoarchitecture of rutile TiO2 nanoneedle/graphene for advanced lithium-ion batteries, Solid State Ionics 269 (2015) 44-50.

[12] M. Breysse, P. Afanasiev, C. Geantet, M. Vrinat, Overview of support effects in hydrotreating catalysts, Catal. Today 86 (2003) 5-16.

[13] A. A. Ismail, D. W. J. Bahnemann, D. W. Mesoporous titania photocatalysts: preparation, characterization and reaction mechanisms, J. Mater. Chem. 21 (2011) 11686-11707.

[14] N. B. Lihitkar, M. K. Abyaneh, V. Samuel, R. Pasricha, S. W. Gosavi, S. K. Kulkarni, Titania nanoparticles synthesis in mesoporous molecular sieve MCM-41, J. Colloid. Interface Sci. 314 (2007) 310-316.

[15] M. Besançon, L. Michelin, L. Josien, L. Vidal, K. Assaker, M. Bonne, B. Lebeau, J.L. Blin J.L., Influence of the porous texture of SBA-15 mesoporous silica on the anatase formation in TiO_2-SiO_2 nanocomposites, New J. Chem. 40 (2016) 4386-4397.

[16] A. A. Cecilio, S. H. Pulcinelli, C. V. Santilli, Y. Maniette, Improvement of the Mo/TiO_2-Al_2O_3 catalyst by the control of the sol-gel synthesis, J. Sol-Gel Sci. Technol. 31 (2004) 87-93.

[17] L. Chao, Z. Zhiming, H. Yongli, C. Zhenmin, Y. Weikang, Support effects on Thiophene hydrodesulfurization over Co-Mo-Ni/Al_2O_3 and Co-Mo-Ni/TiO_2-Al_2O_3 Catalysts, Chin. J. Chem. Eng., 22 (2014) 383-391.

[18] M. E. Simonsen, E. G. Søgaard, Sol–gel reactions of titanium alkoxides and water: influence of pH and alkoxy group on cluster formation and properties of the resulting products, J. Sol-Gel Sci. Technol. 53 (2010) 485-497.

[19] T. Kimura, Evaporation-induced self-assembly process controlled for obtaining highly ordered mesoporous materials with demanded morphologies, Chem. Rec. 16 (2016) 445-457.

[20] B. P. Bastakoti, S. Ishihara, S. Y. Leo, K. Ariga, K. C.-W. Wu, Y. Yamauchi, Polymeric micelle assembly for preparation of large-sized mesoporous metal oxides with various compositions, Langmuir 30 (2014) 651-659.

[21] B. P. Bastakoti, Y. Li, M. Imura, N. Miyamoto, T. Nakato, T. Sasaki, Y. Yamauchi, Polymeric micelle assembly with inorganic nanosheets for construction of mesoporous architectures with crystallized walls, Angew. Chem. Int. Ed. 54 (2015) 4222 -4225.

[22] H. Oveisi, S. Rahighi, X. Jiang, Y. Nemoto, A. Beitollahi, S. Wakatsuki, Y. Yamauchi, Unusual antibacterial property of mesoporous titania films: drastic improvement by controlling surface area and crystallinity, Chem. Asian J. 5 (2010) 1978-1983.

[23] D. P. Debecker, S. Le Bras, C. Boissière, A. Chaumonnot, C. Sanchez, Aerosol processing: a wind of innovation in the field of advanced heterogeneous catalysts, Chem. Soc. Rev. 47 (2018) 4112-4155.

[24] S. Bagheri, Z. A. M. Hir, A. T. Yousefi, S. B. A. Hamid, Progress on mesoporous titanium dioxide: synthesis, modification and applications, Microporous Mesoporous Mater. 218 (2015) 206-222.

[25] S. Y. Choi, M. Mamak, N. Coombs, N. Chopra, G. A. Ozin, Thermally stable two-dimensional hexagonal mesoporous nanocrystalline anatase, Meso-nc-TiO_2: bulk and crack-free thin film morphologies, Adv. Funct. Mater. 14 (2004) 355-344.

[26] D. L. Li, H. S. Zhou, I. Homma, Design and synthesis of self-ordered mesoporous nanocomposite through controlled in-situ crystallization, Nat. Mater. 3 (2004) 65-72.

[27] W. Dong, Y. Sun, C. W. Lee, W. Hua, X. Lu, Y. Shi, S. Zhang, J. Chen, D. Zhao, Controllable and repeatable synthesis of thermally stable anatase nanocrystal-silica composites with highly ordered hexagonal mesostructures, J. Am. Chem. Soc. 129 (2007) 13894-13904.

[28] W. Dong, Y. Sun, Q. Ma., L. Zhu, W. Hua, X. Lu, G. Zhuang, S. Zhang, Z. Guo, D. Zhao, Excellent photocatalytic degradation activities of ordered mesoporous anatase TiO_2–SiO_2 nanocomposites to various organic contaminants, J. Hazardous Mater. 229-230 (2012) 307-320.

[29] W. Dong, Y. Yao, L. Li, Y. Sun, W. Hua, G. Zhuang, D. Zhao, S. Yan, W. Song, Three-dimensional interconnected mesoporous anatase TiO_2 exhibiting unique photocatalytical performance. Appl. Catal. B: Environmental 217 (2017) 293-302.

[30] L. Körösi, S. Papp, I. Bertóti, I. Dékány, Surface and bulk composition, structure, and photocatalytic activity of phosphate-modified TiO_2, Chem. Mater. 19 (2007) 4811-4819.

[31] Y. Zhang, H. Zhang, Y. Xu, Y. Wang, Significant effect of lanthanide doping on the texture and properties of nanocrystalline mesoporous TiO_2, J. Solid State Chem. 177 (2004) 3490-3498.

[32] H. Oveisi, X. Jiang, Y. Nemoto, A. Beitollahi, Y. Yamauchi, Cerium-doped mesoporous TiO_2 thin films: Controlled crystallization of anatase with retention of highly ordered mesostructure, Microporous Mesoporous Mater. 139 (2011) 38-44.

[33] J. Xiao, T. Peng, R. Li, Z. Peng, C. Yan, Preparation, phase transformation and photocatalytic activities of cerium-doped mesoporous titania nanoparticles, J. Solid State Chem. 179 (2006) 1161-1170.

[34] S. Vargas, R. Arroyo, E. Haro, R. Rodríguez, Effects of cationic dopants on the phase transition temperature of titania prepared by the sol-gel method, J. Mater. Res. 14 (1999) 3932-3937.

[35] H. Oveisi, A. Beitollahi, X. Jiang, K. Sato, Y. Nemoto, N. Fukata, Y. Yamauchi, synthesis of continuous mesoporous Ga-doped titania films with anatase crystallized framework, J. Nanosci. Nanotechnol.11 (2011) 6926-6933.

[36] J. Kim, K.C. Song, S. Foncillas, S.E. Pratsinis, Dopants for synthesis of stable bimodally porous titania, J. Eur. Ceram. Soc. 21 (2001) 2863-2872.

[37] T. D. Nguyen-Phan, M. B. Song, E. J. Kim, E. W. Shin, The role of rare earth metals in lanthanide-incorporated mesoporous titania, Microporous Mesoporous Mater. 119 (2009) 290-298.

[38] K. Zimny, J. Ghanbaja, C. Carteret, M.-J. Stébé, J.-L. Blin, Highly ordered mesoporous titania with semi crystalline framework templated by large or small nonionic surfactants, New. J. Chem. 34 (2010) 2113-2117.

[39] K. Zimny, T. Roques-Carmes, C. Carteret, M.-J. Stébé, J.-L. Blin, Synthesis and photoactivity of ordered mesoporous titania with a semicrystalline framework, J. Phys. Chem. C 116 (2012) 6585-6594.

[40] A. M. Mohammed, M. Sebek, C. Kreyenschulte, H. Lund, J. Rabeah, P Langer, J. Strunk, N. Steinfeldt, Effect of metal ion addition on structural characteristics and photocatalytic activity of ordered mesoporous titania, J. Sol-Gel Sci. Technol. 91 (2019) 539-551.

[41] I. Naboulsi, B. Lebeau, L. Michelin, C. Carteret, M. Bonne, J.-L. Blin, Influence of crystallization conditions and of gaseous ammonia treatment on mesoporous TiO_2 properties, Microporous and Mesoporous Mater. 262 (2018) 1-12.

[42] E. P. Barrett, L. G. Joyner, P. P. Halenda, The determination of pore volume and area distributions in porous substances. I. Computations from nitrogen isotherms, J. Am. Chem. Soc. 73 (1951) 373-380.

[43] M. Kruk, M. Jaroniec, A. Sayari, Adsorption Study of Surface and Structural Properties of MCM-41 Materials of Different Pore Sizes, Chem. Mater. 11 (1999) 492-500.

[44] Z.W. Seh, S. Liu, M. Low, S. Y. Zhang, Z. Liu, A. Mlayah, M. Y. Han, Janus Au-TiO_2 Photocatalysts with Strong Localization of Plasmonic Near-Fields for Efficient Visible-Light Hydrogen Generation, Adv. Mater. 24 (2012) 2310-2314.

[45] B. Luo, Z. Li, Y. Xu, The positive effect of anatase and rutile on the brookite-photocatalyzed degradation of phenol, RSC Adv. 5 (2015) 105999-106004.

[46] S. Kelly, F. H. Pollak, M. Tomkiewicz, Raman spectroscopy as a morphological probe for TiO_2 aerogels, J. Phys. Chem. B 101 (1997) 2730-2734.

[47] A. Mattsson, L. Österlund, Phys. Chem. C, Adsorption and photoinduced decomposition of acetone and acetic acid on anatase, brookite, and rutile TiO_2 nanoparticles 114 (2010) 14121-14132.

[48] K. Cassiers, T. Linssen, M. Mathieu, Y. Q. Bai, H. Y. Zhu, P. Cool, E. F. Vansant, Surfactant-directed synthesis of mesoporous titania with nanocrystalline anatase walls and remarkable thermal stability, J. Phys. Chem. B 108 (2004) 3713-3721.

[49] M. Thommes, K. Kaneko, A. V. Neimark, J. P. Olivier, F. Rodriguez-Reinoso, J. Rouquerol, K. S. W. Sing, Physisorption of gases, with special reference to the evaluation of surface area and pore size distribution (IUPAC Technical Report), Pure Appl. Chem. 87 (2015) 1051–1069.

[50] P. Periyat, K. V. Baiju, P. Mukundan, P. K. Pillai, K. G. K. Warrier, High temperature stable mesoporous anatase TiO_2 photocatalyst achieved by silica addition, Appl. Catal., A 349 (2008) 13-19.

[51] D. Massiot, F. Fayon, M. Capron, I. King, S. Le Calvé, B. Alonso, J. O. Durand, B. Bujoli, Z. Gan, G. Hoatson**,** Modelling one and two-dimensional solid-state NMR spectra*,* Magn. Reson. Chem. 40 70-76 (2002)

[52] C. Schmutz P. Barboux, F. Ribot, F. Taulelle, M. Verdaguer, C. Fernandez-Lorenzo, EXAFS, Raman and ^{31}P NMR study of amorphous titanium phosphates, J. Non-Cryst. Solids 170 (1994) 250-262

[53] K. Elghniji, M. El Khames Saad, M. Araissi, E. Elaloui, Y. Moussaoui, Chemical modification of TiO2 by H2PO4−/HPO42− anions using the sol-gel route with controlled precipitation and hydrolysis: enhancing thermal stability, Mater. Sci.-Poland, 32 (2014) 617-625.

[54] A. Estrella González, M. Asomoza, U. Arellano, S. Cipagauta Díaz, S. Solís, Preparation and characterization of phosphate-modified mesoporous TiO_2 incorporated in a silica matrix and their photocatalytic properties in the photodegradation of Congo red, Front. Mater. Sci. **11** (2017) 250–261.

[55] P. A. Connor, A. J. McQuillan, Phosphate adsorption onto TiO2 from aqueous solutions: An in situ internal reflection infrared spectroscopic study, Langmuir, 15 (1999) 2916-2921.

[56] K. Okada, N. Yamamoto, Y. Kameshima, A. Yasumori, K. J. D. MacKenzie, Effect of Silica Additive on the Anatase-to-Rutile Phase Transition, J. Am. Ceram. Soc., 84 (2001) 1591-1596.

[57] G. W. Wallidge, R. Anderson, G. Mountjoy, D. M. Pickup, P. Gunawidjaja, R. J. Newport, M. E. Smith, Advanced physical characterisation of the structural evolution

of amorphous $(TiO_2)(x)(SiO_2)(1-x)$ sol-gel materials, J. Mater. Sci., 39 (2004) 6743-6755.

[58] L. A. O'Dell, S. L. P. Savin, A. V. Chadwick, M. E. Smith, A ^{27}Al MAS NMR study of a sol–gel produced alumina: Identification of the NMR parameters of the θ-Al_2O_3 transition alumina phase, Solid State Nucl. Magn. Reson. 31 (2007) 169-173.

[59] E. W. Hagaman, J. Jiao, B. Chen, Z. Ma, H. Yin, S. Dai, Surface alumina species on modified titanium dioxide: A solid-state Al-27 MAS and 3QMAS NMR investigation of catalyst supports, Solid State Nuclear Magnetic Res. 37 (2010) 82-90.

[60] L. A. O'Dell, S. L. P. Savin, A. V. Chadwick, M. E. Smith, Structural Characterization of SiO_2 and Al_2O_3 Zener-Pinned Nanocrystalline TiO_2 by NMR, XRD and Electron Microscopy, J. Phys. Chem. C 2007, 111, 13740-13746

[61] W. M. Haynes, D. R. Lide, T. J. Bruno, CRC Handbook of Chemistry and Physics, 97th ed., CRC Press, Taylor & Francis Group, Boca Raton, FL, 2016-2017, PP 12-12.

[62] A. Kitiyanan, T. Kato, Y. Suzuki, S. Yoshikawa, The use of binary TiO_2–GeO_2 oxide electrodes to enhanced efficiency of dye-sensitized solar cells, J. Photochem. Photobiol., A 179 (2006) 130-134.

[63] R. Liu, Y. Ren, Y. Shi, F. Zhang, L. Zhang, B. Tu, Controlled synthesis of ordered mesoporous C–TiO_2 nanocomposites with crystalline titania frameworks from organic–inorganic–amphiphilic coassembly, Chem. Mater. 20 (2008) 1140-1146

[64] W. Zhou, F. Sun, K. Pan, G. Tian, B. Jiang, Z. Ren, C. Tian, H. Fu, Well-ordered large-pore mesoporous anatase TiO_2 with remarkably high thermal stability and improved crystallinity: preparation, characterization, and photocatalytic performance, Adv. Func. Mater. 21 (2011) 1922-1930.

[65] J.C. Yu, L. Zhang, Z. Zheng, J. Zhao, Synthesis and Characterization of Phosphated Mesoporous Titanium Dioxide with High Photocatalytic Activity, Chem. Mater. 15 (2003) 2280-2286.

[66] H. Limin, L. Quanzhi, Enhanced acidity and thermal stability of mesoporous materials with post-treatment with phosphoric acid, Chem. Lett. 28 (1999) 829-830.

[67] S.M. Hassan, M. A. Mannaa, A. A. Ibrahim, Nano-sized mesoporous phosphated tin oxide as an efficient solid acid catalyst, RSC. Adv. 9 (2019) 810-818.

[68] L. Atanda, S. Mukundan, A. Shrotri, Q. Ma, J. Beltramini, Catalytic conversion of glucose to 5-hydroxymethyl-furfural with a phosphated TiO_2 catalyst, ChemCatChem. 5 (2015) 781-790.

[69] R. Rodríguez-Talavera, S. Vargas, R. Arroyo-Murillo, R. Montiel-Campos, E. Haro-Poniatowski, Modification of the phase transition temperatures in titania doped with various cations, J. Mater. Res. 12 (1997) 439-443.

[70] S. Vargas, R. Arroyo, E. Haro, R. Rodríguez, Effects of cationic dopants on the phase transition temperature of titania prepared by the sol-gel method, J. Mater. Res. 14 (1999) 3932-3937.

[71] F. Huang, M. Zhou, Y. B. Cheng, R. A. Caruso, Al-containing porous titanium dioxide networks: sol-gel synthesis within agarose gel template and photocatalytic activity, Chem. Mater. 18 (2006) 5835-5839.

[72] N Khatun, S. Tiwari, C. P. Vinod, C. M. Tseng, S. W. Liu, S. Biring, S. Sen, Role of oxygen vacancies and interstitials on structural phase transition, grain growth, and optical properties of Ga doped TiO_2, J. Appl. Phys. 123 (2018) 1-10.

[73] S. Luo, T. D. Nguyen-Phan, D. Vovchok, I. Waluyo, R. M. Palomino, A. D. Gamalski, L. Barrio, W. Xu, D. E. Polyansky, J.A. Rodriguez, S.D. Senanayake, Enhanced,

robust light-driven H_2 generation by gallium-doped titania nanoparticles, Phys. Chem. Chem. Phys. 20 (2018) 2104-2112.

[74] V. Štengl, J. Henych, M. Slušná, T.M. Grygar, J. Velická, M. Kormunda, Improvement of orange II photobleaching by Moderate Ga^{3+} doping of titania and detrimental effect of structural disorder on Ga overloading, J. Nanomater. 6 (2014) 1-11.

[75] J. Yang, J. M. F. Ferreira, On the titania phase transition by zirconia additive in a sol-gel-derived powder, Mater. Res. Bull. 33 (1998) 389-394.

[76] W. Zhou, K. Liu, H. Fu, K. Pan, L. Zhang, L. Wang, C.C. Sun, Multi-modal mesoporous TiO_2–ZrO_2 composites with high photocatalytic activity and hydrophilicity, Nanotechnology 19 (2008) 035610.

[77] J. C. Yu, J. Lin, R. W. M. Kwok, $Ti_{1-x}Zr_xO_2$ solid solutions for the photocatalytic degradation of acetone in air, J. Phys. Chem. B 102 (1198) 5094-5098.

Table 1: Collapse temperature (T_C) of the mesostructure, temperature of crystallization into nano-size anatase determined from XRD (T_A), temperature at which the rutile polymorph is detected by XRD (T_R) and ionic radius (R_i) of the heteroelement for a coordination number equal to 6 [61].

Heteroelement	T_C (°C)	T_A (°C)	T_R (°C)	R_i (Å)
None	600	380 (380)[$]	700	0.61 (Ti^{4+})
PO_4^{3-}/P^{5+}	800	600 (600) [$]	-	2.38*/0.38[#]
Si^{4+}	800	600 (600) [$]	-	0.40
Al^{3+}	700	600 (500) [$]	900	0.54
Ge^{4+}	700	500 (500) [$]	700	0.53
Ga^{3+}	600	380 (380) [$]	900	0.62
Zr^{4+}	600	600 (500) [$]	900	0.72

[$]values in brackets correspond to the temperature at which the anatase phase is observed by Raman spectroscopy
[*]thermochemical ionic radius from A.F. Kapustinski, Quart. Rev., 1956, 10, 286.
[#]ionic radius of P^{5+} for a coordination number equal to 6 from ref. 61.

Table 2: Crystallite sizes of anatase (nm) determined with Scherrer equation after heating the extracted TiO_2 at different temperatures.

Heating Temperature (°C)	Bare TiO_2	PO_4^{3-}	Si^{4+}	Al^{3+}	Ge^{4+}	Ga^{3+}	Zr^{4+}
380	4	-	-	-	-	5	-
500	14	-	-	-	5 **β**	10	-
600	18(17)*	4 **β**	2 **β**	7	8 **β**	15	11
700	71 **R**	6 **β**	4 **β**	11(10)*	20(15)*R	25(14)*	14 **Zr**
800	543 **R**	16(13)*	8(6)* **β**	24 **R**	50 **R**	47 **Ga**	17 **Zr**
900	291 **R**	83 **P**	13	76 **R**	106 **R**	180 **R, Ga**	37 **Zr, R**

- no anatase particle is detected by XRD
*value in bracket corresponds to the average particle size determined from TEM images (about 20 measurements)
R : rutile
β : β-TiO_2
P : TiP_2O_7
Ga : Ga_2O_3
Zr : Ti_2ZrO_6 or Brookite

Table 3: Mesopore diameter (nm) of the titania materials containing heteroelement and heating at different temperatures after extraction. Diameter have been obtained by applying the BJH method with KJS correction to the adsorption branch of the isotherm.

Heating temperature (°C)	Bare TiO_2	PO_4^{3-}	Si^{4+}	Al^{3+}	Ge^{4+}	Ga^{3+}	Zr^{4+}
Extracted	9.4	9.4/11.0	8.7	9.8/11.0	9.8/11.5	10.7	7.7
380	8.9	6.5/10.1	7.3	7.5/10.3	10.3	8.7	6.1
500	7.2	7.1/9.9	7.7	8.3/10.0	7.6	7.8	6.1
600	6.7	6.6/7.8	6.3	6.5/8.2	6.6	6.8	6.5
700	-	5.6/6.4	6.2	8.9	7.8	10.1	10.0
800	-	11.0	5.6	12.0	-	-	15.1
900	-	12.6	5.4	-	-	-	-

- : no maximum in the mesopore domain

Figures caption

Figure 1: Plot of the correlation distance corresponding to the broad SAXS peak at low q (Fig. S1) versus the anatase crystallite size determined with Scherrer equation (Table 2).

Figure 2: SEM (1st and 3rd columns. Scale bars = 100 nm) and TEM (2nd and 4th columns. Scale bars = 50 nm) images of all materials calcined at 380°C and of bare TiO_2 calcined at 600°C, of TiO_2 containing Al^{3+}, Ge^{4+}, Ga^{3+} and Zr^{4+} calcined at 700 °C, and of TiO_2 doped with Si^{4+} and PO_4^{3-} calcined at 800°C.

Figure 3: Variation of the pore volume (A) and of the specific surface area (B) as a function of the heating temperature of mesostructured titania prepare without and in the presence of heteroelement.

Figure 4: Mesopores size distribution, obtained from the BJH method with KJS correction applied to the adsorption branch of the isotherm, as a function of the heating temperature of mesostructured titania prepared in the presence of heteroelements.

Figure 5: A) ^{31}P MAS spectra of Ti containing PO_4^{3-} calcined at 380, 600, 800 and 900°C, B) ^{29}Si CP-MAS spectra of Ti containing Si^{4+} calcined at 380, 600 and 800°C, and C) ^{27}Al MAS spectra of Ti containing Al^{3+} calcined at 380, 600, 800 and 900°C

Figure 1

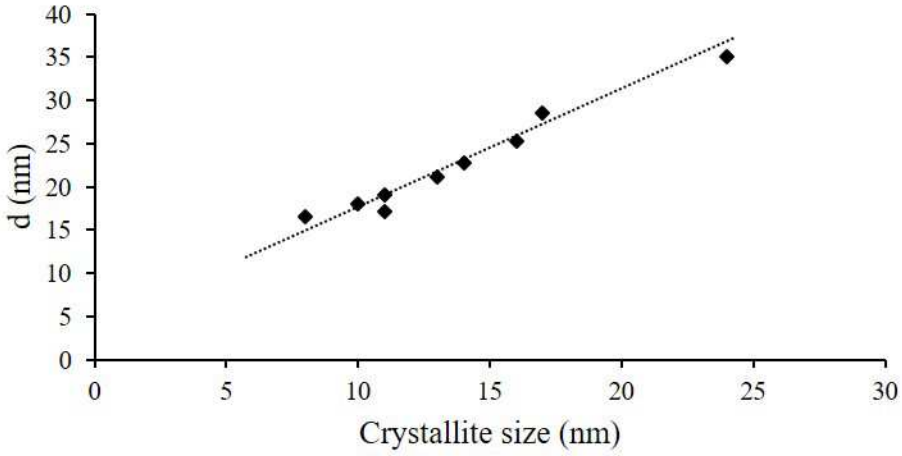

Figure 2

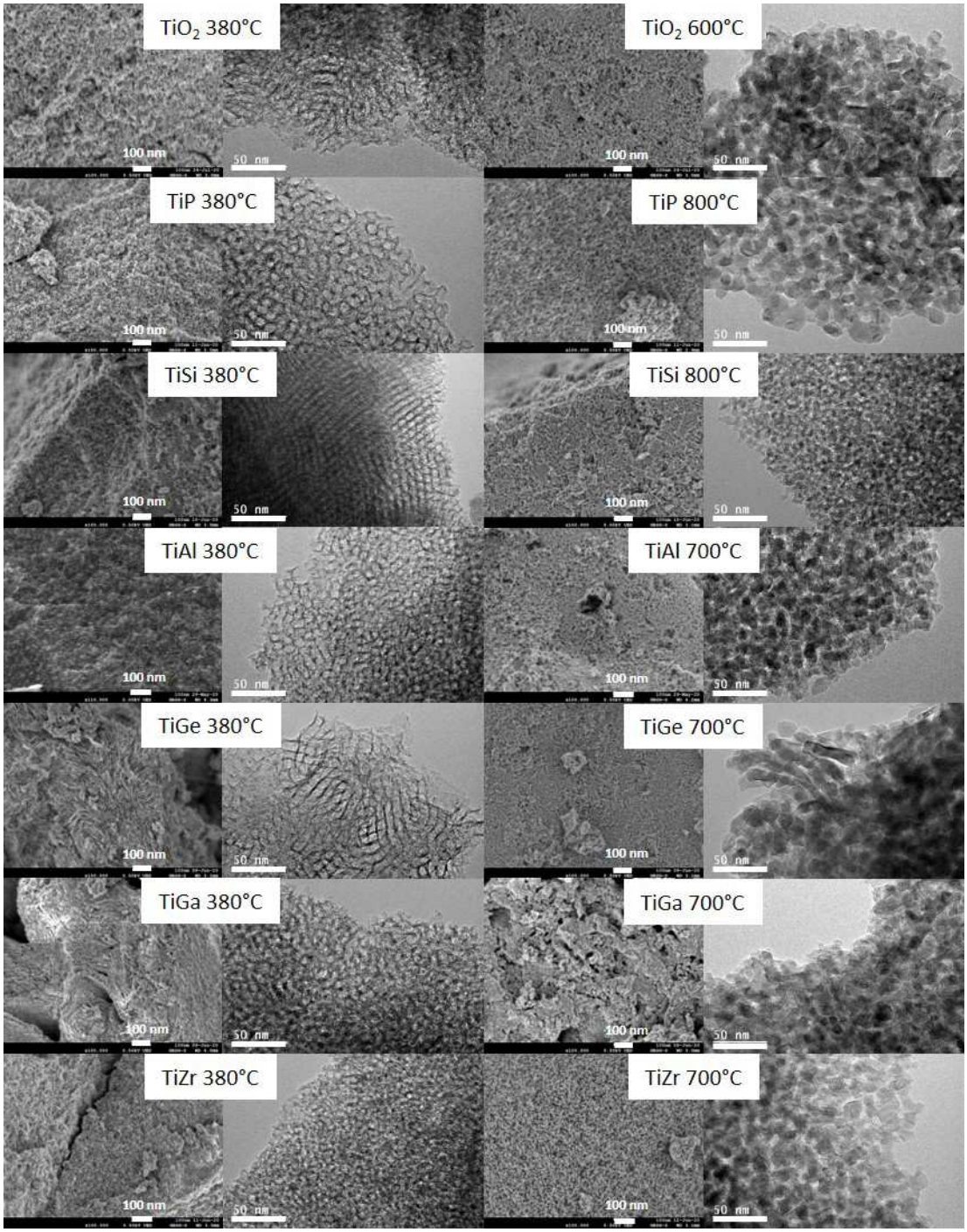
TiO2 380°C
TiO2 600°C
TiP 380°C
TiP 800°C
TiSi 380°C
TiSi 800°C
TiAl 380°C
TiAl 700°C
TiGe 380°C
TiGe 700°C
TiGa 380°C
TiGa 700°C
TiZr 380°C
TiZr 700°C
100 nm
50 nm

Figure 3

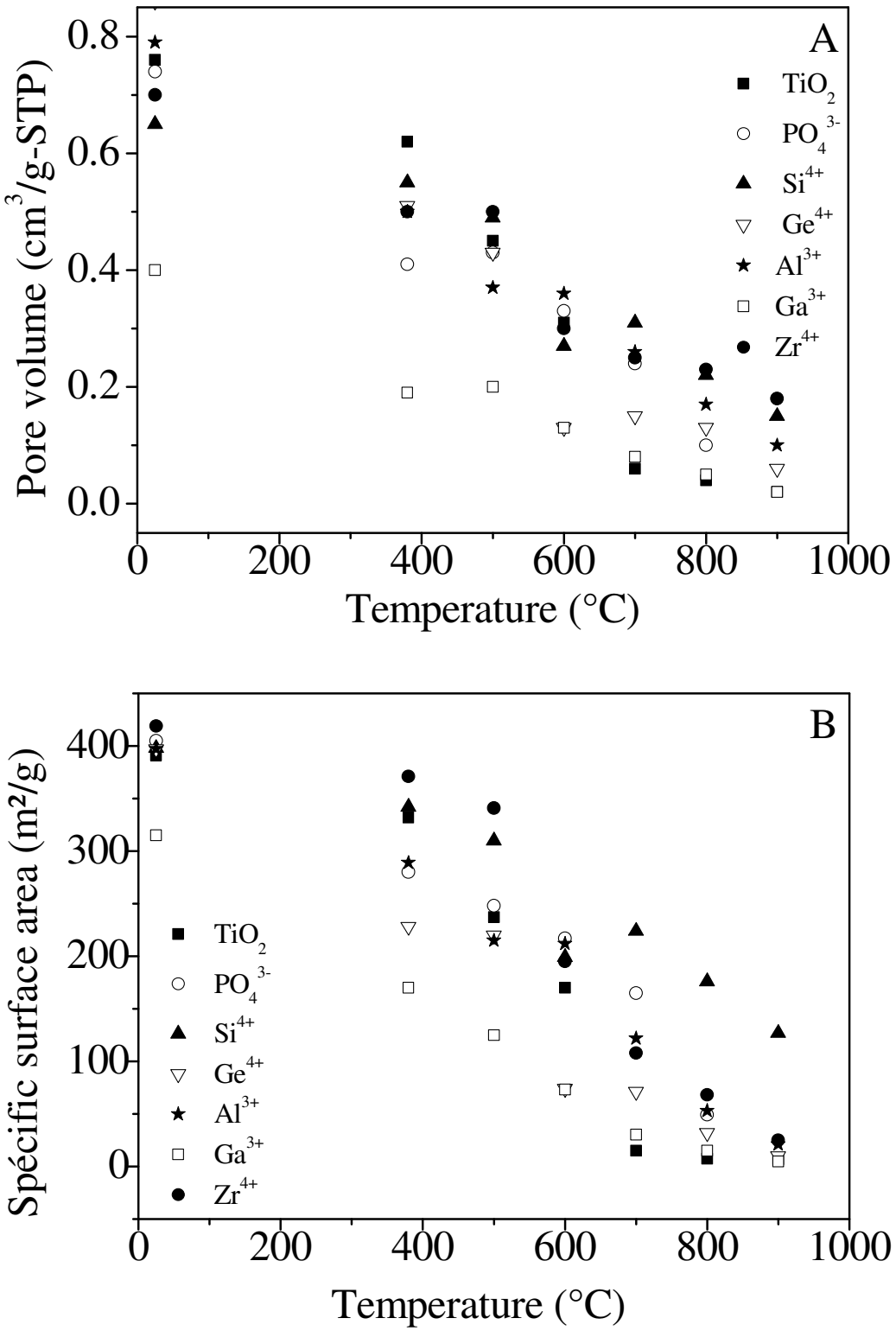
A
Pore volume (cm³/g-STP)
0.0
0.2
0.4
0.6
0.8
0
200
400
600
800
1000
Temperature (°C)
TiO2
PO4 3-
Si4+
Ge4+
Al3+
Ga3+
Zr4+
B
Spécific surface area (m²/g)
0
100
200
300
400
0
200
400
600
800
1000
Temperature (°C)
TiO2
PO4 3-
Si4+
Ge4+
Al3+
Ga3+
Zr4+

Figure 4

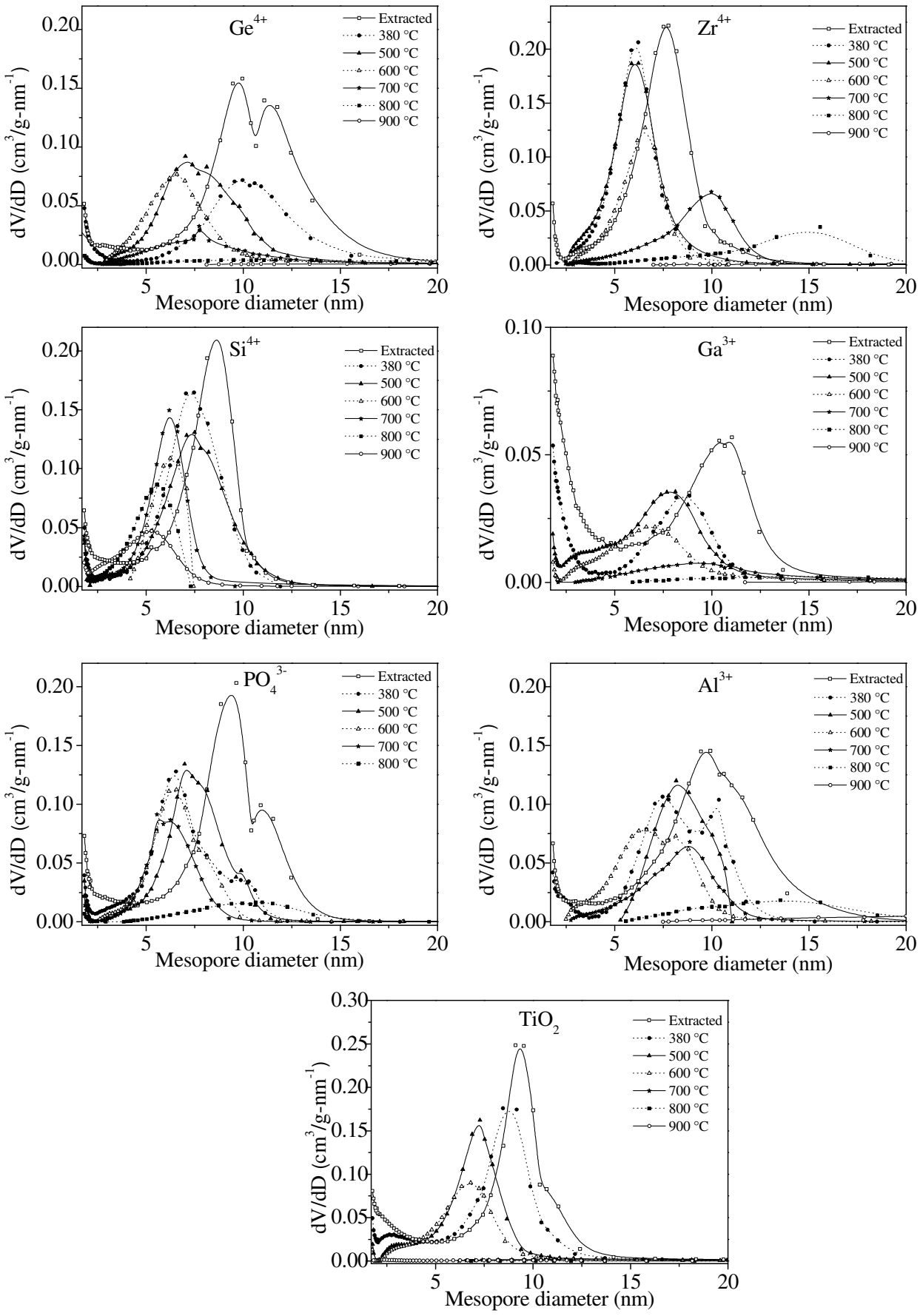
Ge4+
Zr4+
Si4+
Ga3+
PO4 3-
Al3+
TiO2
Extracted
380 °C
500 °C
600 °C
700 °C
800 °C
900 °C
dV/dD (cm3/g-nm-1)
Mesopore diameter (nm)

Figure 5

A

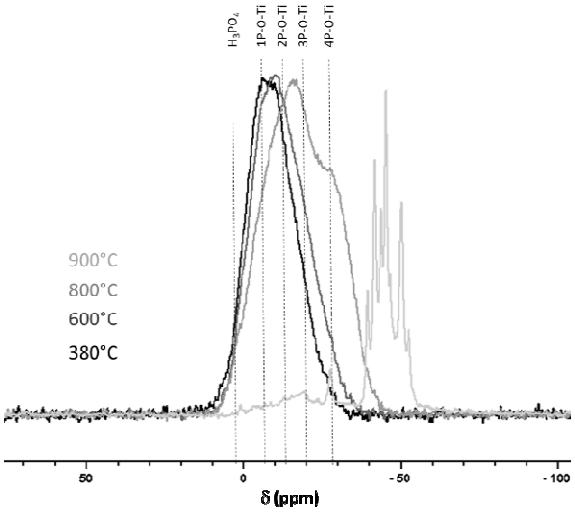
H3PO4
1P-O-Ti
2P-O-Ti
3P-O-Ti
4P-O-Ti
900°C
800°C
600°C
380°C
50
0
-50
-100
δ (ppm)

B

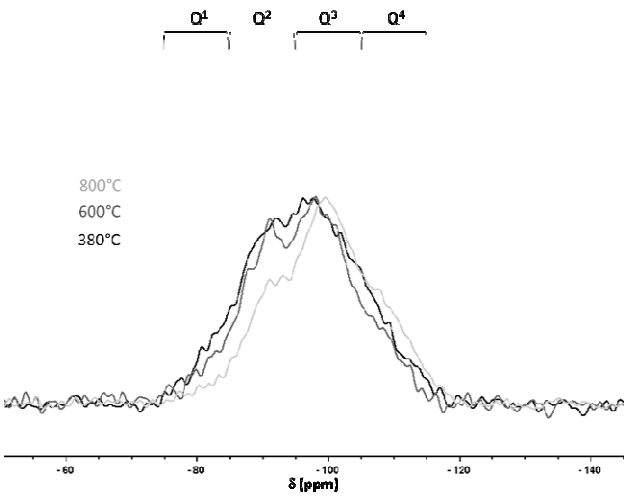
Q1
Q2
Q3
Q4
800°C
600°C
380°C
-60
-80
-100
-120
-140
δ (ppm)

C

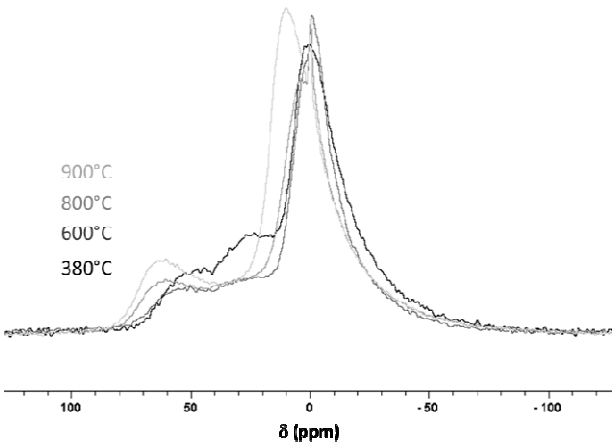
900°C
800°C
600°C
380°C
100
50
0
-50
-100
δ (ppm)